CHEMISTRY

A multifunctional surfactant catalyst inspired by hydrolases

Mitchell D. Nothling[1], Zeyun Xiao[2], Nicholas S. Hill[3], Mitchell T. Blyth[3], Ayana Bhaskaran[3], Marc-Antoine Sani[4], Andrea Espinosa-Gomez[1], Kevin Ngov[1], Jonathan White[4], Tim Buscher[5], Frances Separovic[4], Megan L. O'Mara[3], Michelle L. Coote[6], Luke A. Connal[3]*

The remarkable power of enzymes to undertake catalysis frequently stems from their grouping of multiple, complementary chemical units within close proximity around the enzyme active site. Motivated by this, we report here a bioinspired surfactant catalyst that incorporates a variety of chemical functionalities common to hydrolytic enzymes. The textbook hydrolase active site, the catalytic triad, is modeled by positioning the three groups of the triad (-OH, -imidazole, and -CO_2H) on a single, trifunctional surfactant molecule. To support this, we recreate the hydrogen bond donating arrangement of the oxyanion hole by imparting surfactant functionality to a guanidinium headgroup. Self-assembly of these amphiphiles in solution drives the collection of functional headgroups into close proximity around a hydrophobic nano-environment, affording hydrolysis of a model ester at rates that challenge α-chymotrypsin. Structural assessment via NMR and XRD, paired with MD simulation and QM calculation, reveals marked similarities of the co-micelle catalyst to native enzymes.

INTRODUCTION

The impressive catalytic power of enzymes, as well as their remarkable stereo-, regio- and substrate specificity, has underpinned the evolution of life on Earth. Much research has been directed at elucidating the structure and function of enzymes, and it is now well accepted that many enzymes use a complex suite of covalent, electrostatic, hydrogen bonding (H-bonding), and directional interactions to undertake catalysis (*1*–*7*). Notably, it is the well-defined combination of multiple chemical interactions within the enzyme protein structure that gives rise to their unrivalled rate enhancement (*8*). In the study of enzyme function and in the development of new catalysts, a major target for researchers has been the design of simpler, small-molecule enzyme models that incorporate one or more of these interactions. An understanding that enzymes, as Knowles (*9*) suggests, are "not different, just better" has driven the exploration of such model materials, although the realization of substantial reaction rate enhancements remains extremely challenging. The field of enzyme mimicry based on active-site structure has been widely examined, with pioneering work by Breslow (*10*), Cram (*11*, *12*), and Rebek (*13*) and their co-workers introducing the idea of synthetic binding pockets that may attract and partition substrates similarly to native enzymes (*14*).

Hydrolytic enzymes (hydrolases) as an enzyme family have received significant focus due to their ubiquity in living systems and their increasing industrial relevance (*15*, *16*). In particular, the serine proteases are an important hydrolase class that have been the target of enzyme-mimicking efforts, with the digestive protease α-chymotrypsin an illustrative example of controlling multiple chemical interactions (*10*, *17*–*19*). At the core of the protein structure lies a relatively small functional area, the active site, which mediates their important reactions. The active site of chymotrypsin-like hydrolases is often composed of a hydrophobic binding pocket that contains three spatially close amino acid residues, histidine, aspartate, and serine, known as the catalytic triad (*20*, *21*). In addition, the important functional role of the active-site residues is frequently supported by nearby complementary residues that participate in H-bonding with reaction intermediates and transition states to reduce the activation energy of the catalytic reaction. In many serine proteases, two nearby peptide N—H moieties undertake this role in a region known as the oxyanion hole (*22*). The combination of a hydrophobic pocket, the catalytic triad residues, and the oxyanion hole in the hydrolases collectively affords hydrolysis of select substrates at rates approaching the diffusion limit (*23*). A long-standing challenge for researchers is to imitate the unique structural features of hydrolases in a synthetic catalyst system. Progress in synthetic polymer chemistry has afforded abiotic macromolecules that can self-assemble to afford unique internal environments and functionalities, similar to native enzymes (*24*–*26*). In particular, the collapse or folding of polymeric chains—termed foldamers—into single-chain nanoparticles represents a powerful approach to mimic the tertiary structure of biopolymers (*27*, *28*). However, the influence of synergizing multiple chemical and physical interactions into an effective catalyst design remains mostly an open question (*26*).

The challenge we have targeted is to combine these multiple enzyme properties—the active-site chemistry, hydrophobic environment, and transition-state stabilization—into a single enzyme-inspired catalytic system. We do this by using the ubiquitous method of self-assembling amphiphiles to recreate the macromolecular architecture of enzymes by forming micelles. Micellar catalysis has been an active research area, including work that aims to mimic the hydrophobic binding pocket of enzymes with the internal, low-polarity environment of micelles (*29*–*32*). Early work by Kunitake *et al.* (*33*, *34*), Ihara *et al.* (*35*), and Tonellato (*36*, *37*) illustrated the benefit of functionalized surfactant headgroups for undertaking both inter- and intramolecular cooperative catalysis. However, to the best

[1]Department of Chemical and Biomolecular Engineering, The University of Melbourne, Melbourne, VIC 3010, Australia. [2]Chongqing Institute of Green and Intelligent Technology, Chinese Academy of Sciences, Chongqing 400714, P. R. China. [3]Research School of Chemistry, Australian National University, Canberra, ACT 2601, Australia. [4]School of Chemistry, Bio21 Institute, The University of Melbourne, Melbourne, VIC 3010, Australia. [5]Department of Chemistry and Biochemistry, University of California, Santa Barbara, Santa Barbara, CA 93106, USA. [6]ARC Centre of Excellence for Electromaterials Science, Research School of Chemistry, Australian National University, Canberra, ACT 2601, Australia.
*Corresponding author. Email: luke.connal@anu.edu.au

of our knowledge, no previous study has combined the three groups of the catalytic triad into the headgroup of a surfactant—and furthermore including transition-state stabilization groups into a co-micellar system. Herein, we report a bioinspired catalyst that contains an imidazole, a hydroxyl, and a carboxylate group in close proximity on a single molecule to give an artificial catalytic triad (ACT) (Fig. 1). The simple, high-yielding, and modular synthesis allows fine adjustment to the relative positioning of the catalytic functional groups, yielding a surfactant-type molecule with a catalytic triad functionalized headgroup that can form a co-micelle capsule in solution. Furthermore, inspired by the active site of native enzymes, which is supported by an oxyanion hole, these ACT surfactants have then been coassembled with a guanidine headgroup 16-carbon surfactant. Such a cosurfactant is capable of donating strong, bifurcated H-bonding and is critical to assist the ACT in catalysis by undertaking supporting interactions with the catalyst-substrate complex. This approach is a simple and scalable synthesis for the creation of a multifunctional, synthetic self-assembled catalytic system inspired by the properties of serine proteases.

RESULTS AND DISCUSSION

We found inspiration in the power of micellar self-assembly to drive the collection of multiple functionalities into a confined environment, analogous to the protein folding of enzymes. In this way, the assembly of surfactants, which contain the functional units associated with hydrolase activity (i.e., hydroxyl, imidazole, carboxylate, and H-bond donors) as headgroup, could direct these units into close proximity to undertake bioinspired catalysis. We reasoned that a loss in ideal functional group placement and rigidity in a micellar system may be compensated by an increased number of active sites and flexibility in catalyst placement. Therefore, our first target was the preparation of a functionalized surfactant containing the three groups of the catalytic triad (Fig. 1A).

To achieve this, we used the readily available amino acid L-serine to provide a primary hydroxyl (as the serine residue does in the natural enzyme; Fig. 1C) and a carboxylate group to act as an activator. Attaching 2-formyl imidazole to the primary amine of L-serine via reductive animation is then used to introduce the third component of the catalytic triad, the basic imidazole unit. This straightforward synthesis quantitatively results in a bioinspired trifunctional molecule (an ACT) with each of the three groups of the catalytic triad positioned in close proximity on the same structure. Addition of surfactant functionality is then achieved via the addition of *n*-hexadeca-1-al to the secondary amine of the ACT by way of a second reductive amination, resulting in a 16-carbon ACT surfactant (ACT-C_{16}) (*38*). This two-step strategy represents a powerful route toward highly functional, enzyme-inspired molecules from readily available starting materials, and its modularity enables fine adjustment to the relative positioning of functional groups.

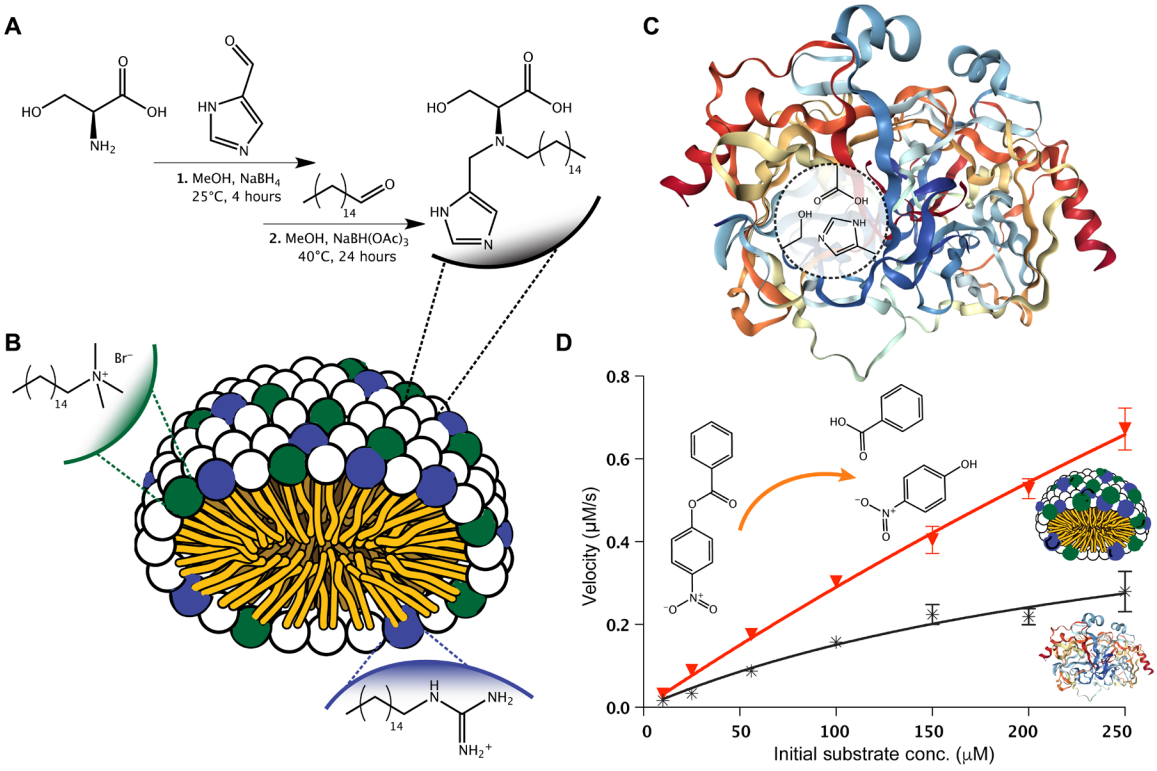

Fig. 1. A hydrolase-inspired cosurfactant catalyst. (**A**) Straightforward preparation of a novel surfactant incorporating an ACT of hydroxyl, carboxylate, and imidazole units as headgroup. (**B**) Self-assembly of the ACT surfactant with cosurfactants [hexadecyl guanidinium hydrochloride (Guan-C_{16}) and cetyltrimethylammonium bromide (CTAB)] yields a functionalized micelle with an internal hydrophobic core as a mimic of native hydrolase binding pockets. (**C**) The active site of a common hydrolase, α-chymotrypsin, highlighting a similar hydrophobic pocket and a catalytic triad of active residues to that of the ACT-surfactant system (*74*). (**D**) The ACT-surfactant coassembly displays an enhanced esterolytic effect for a model substrate when directly compared with the native enzyme α-chymotrypsin. (Data points are the mean of at least three independent experiments, and error bars represent SEM.)

With the active site–inspired ACT-C_{16} in hand, we sought to further extend our design to incorporate a cosurfactant with H-bonding capability as mimicry of the oxyanion hole. We selected guanidine for this role, whose dual N—H bonds are capable of bifurcated H-bond formation, and which has been shown to participate in a variety of nucleophilic and general base catalysis roles, including in native proteins (Fig. 1B) (*39*–*41*). In addition, a guanidine-based surfactant has been shown to increase self-assembly properties due to enhanced H-bond formation between the guanidine headgroups, an advantageous trait to potentially complement the ACT surfactant during catalysis (*42*). The guanidine-containing surfactant hexadecyl guanidinium chloride (Guan-C_{16}) was prepared according to prior literature under mild conditions in quantitative yields, with purification by a single recrystallization step (*43*).

Assessment of the self-assembly of Guan-C_{16} in borate buffer [0.1 M (pH 9.0), 25°C] by the pyrene fluorescence technique revealed a critical micelle concentration (CMC) of 0.28 mM, with the material precipitating at higher concentrations (fig. S1). In contrast, the assessment of the CMC of ACT-C_{16} proved inconclusive because of a low aqueous solubility at room temperature. To address the low solubility of both bioinspired surfactants, we added the common cationic surfactant cetyltrimethylammonium bromide (CTAB) to a buffered mixture of ACT-C_{16} and Guan-C_{16} (ACT-C_{16}:Guan-C_{16}:CTAB = 0.002:0.3:0.8 mM), resulting in a clear solution. These concentrations were selected to (i) ensure micelle formation by targeting a value just above the CMC of both CTAB and Guan-C_{16} and (ii) provide a low, catalytic amount of ACT, such that substrate turnover and saturation kinetics could be targeted during catalytic assessment. The complete dissolution of both bioinspired surfactants on the addition of CTAB provides support for their inclusion into a three-component co-micelle system.

Hydrolysis of a model ester substrate [*p*-nitrophenol benzoate (PNB)] was used to examine the catalytic effect of the three-component surfactant system, which releases the chromogenic product *p*-nitrophenol (Fig. 1D). Enhanced PNB hydrolysis was observed across a broad range of initial substrate concentrations (10 to 250 μM, equating to a catalyst loading of 0.1 to 22 mole percent), with an ACT substrate turnover rate of 1.90 s^{-1} calculated under Michaelis-Menten kinetics (table S1). Compared with the uncatalyzed reaction without any surfactant addition, this represents an approximately 16,000-fold rate enhancement. Excluding any of the three surfactants from the co-micellar assembly resulted in a significantly reduced catalytic effect, particularly when excluding CTAB, which appears pivotal in maintaining solubility of Guan-C_{16} and ACT surfactants. An equivalent concentration of CTAB was added to all assays to ensure a consistent comparison between catalysts, as CTAB can contribute to background ester hydrolysis. Subsequent assessment of the native protease α-chymotrypsin under the same reaction conditions revealed a sevenfold lower substrate turnover rate, highlighting the power of our bioinspired approach under the model conditions. However, the observed Michaelis constant K_M for the enzyme (0.3 mM) is also lower than that for the bioinspired micelle system (1.47 mM). This result may indicate either a lower binding affinity of the micellar catalyst with the ester substrate or an additional contribution of the cosurfactants toward hydrolysis, separate from that undertaken by the ACT. Under the assay conditions, the latter hypothesis would seem more likely, increasing the apparent saturation concentration of the ACT due to the known general base catalysis performed by both CTAB and guanidinium (discussed below). In addition, saturation of the co-micellar construct with the hydrophobic substrate may alter the physical characteristics of the catalytic system, affecting the observed catalysis at higher substrate loading and reducing esterolytic efficiency. It must also be noted that the natural substrate of α-chymotrypsin (proteins, specifically hydrophobic peptide bonds) is decidedly different from the *p*-nitrophenyl model substrate used here, and the basic pH of our assay procedure places the native enzyme at a disadvantage during a direct comparison (*44*, *45*). However, because of convenience for monitoring the hydrolysis spectrophotometrically and the short reaction times, this comparison is frequently made in the literature and provides an insight into the important role of supporting environmental effects for optimizing active-site chemistry. The benzoate ester was examined here as a more stable and challenging model substrate compared with the more commonly explored *p*-nitrophenyl acetate, and the high observed turnover value supports the power of a bioinspired cosurfactant system (*46*).

Active-site mimicry

With the impressive catalytic power of the three-component bioinspired micellar system established, we were drawn to examine the structure and mechanism of the ACT and guanidine surfactants in more detail. First, an examination of the ACT was made to assess the presence of interfunctional group interactions and a mechanism of substrate attack in comparison to the native catalytic triad of α-chymotrypsin. To investigate the participation of the three functional groups of the ACT in catalysis, several control surfactants were prepared and assayed, each excluding a functional group of the ACT (fig. S2). Significantly, a 12-fold reduction in catalytic effect was observed for each of the control structures containing only two functional groups of the ACT when combined with CTAB. This result provides evidence for the concerted action of all three groups during ACT catalysis. However, it must be noted that for the control structure containing imidazole and carboxylate groups (but excluding hydroxyl), an approximately 10% increase in esterolysis was observed above the CTAB background. This finding is consistent with results reported previously where the imidazole unit of histidine can undertake general base hydrolysis of activated substrates (*47*–*49*).

To determine the functional group separation in the ACT, a single crystal of an ACT-C_8 surfactant was grown in water and elucidated via x-ray diffraction (XRD). The solid-phase structure of ACT-C_8 provides information on the functional group interactions (including separation distances), which may affect the solution-phase chemistry of the ACT surfactant. The resolved structure was compared with the well-studied catalytic triad of α-chymotrypsin (Fig. 2, A and B). Similar to the native enzyme, the three functional groups (hydroxyl, imidazolyl, and carboxyl) of the ACT are observed to be spatially close. Intramolecular H-bonding was observed between the carboxyl and imidazolyl groups in the ACT, a phenomenon typical of the enzyme active site. The distance between the carboxyl (O) and imidazolyl (N) of the ACT is 2.72 Å, which is relatively short and is approaching the separation of these groups in the native enzyme (2.64 Å) (*50*). In the native enzyme, however, H-bonding between the Ser-OH and His-N groups is also observed, whereas this was not detected in the solid-state structure of ACT-C_8. This is due to the ACT hydroxyl group forming an intermolecular H-bond with the carboxyl group of a nearby ACT molecule. The interaction between the carboxyl and imidizolyl groups in the ACT occurs between the anti lone pair of the carboxyl-*O* and the imidazolyl-*N* as opposed to

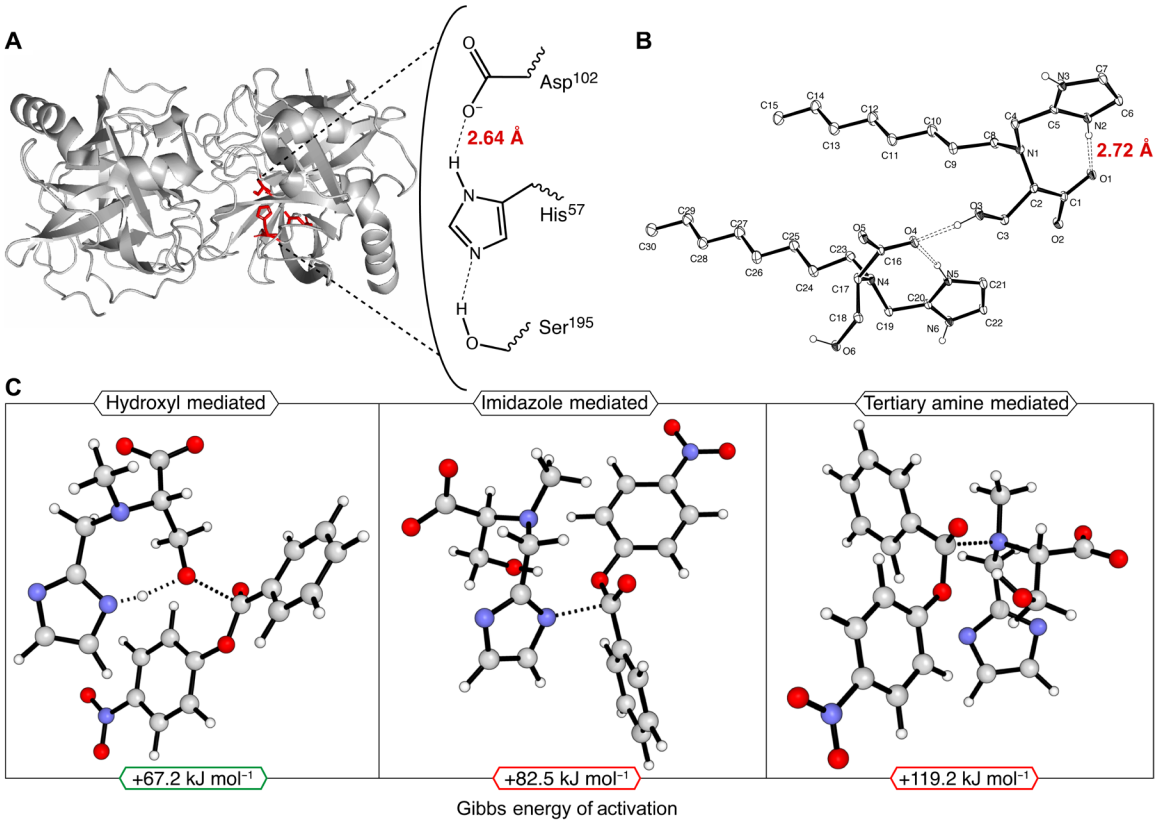

Fig. 2. An ACT. (**A**) The catalytic triad of active-site residues in α-chymotrypsin, highlighting the close proximity of each unit, facilitated by H-bonding (*50*). (**B**) A similarly close proximity of functional groups in the ACT surfactant is observed via single-crystal XRD, emphasizing the power of positioning active groups on a single, trifunctional molecule. (**C**) Assessment of the substrate carbonyl attack by the ACT surfactant (identified as rate-determining) via QM computation reveals a preferred pathway common to native enzymes, whereby the high-energy transition state is established by the nucleophilic ACT hydroxyl group.

the *syn* pair interaction that is observed in the enzyme active site (*51*). The exposed *syn* lone pair of the carboxyl group now has increased basicity due to this interaction, which may provide an alternative method for substrate attack by the ACT via general base catalysis. Further mechanistic alternatives that implicate the imidazole group in nucleophilic attack have also been suggested earlier by Bruice *et al.* (*52*), Johnson (*53*), and Jencks (*54*). Such a mechanism involves substrate carbonyl attack by the imidazolyl-*N*, followed by acyl transfer to water, although the studied systems lack the additional -OH and -COOH functional groups present in the ACT.

To provide further insight into the potential catalytic mechanism of the ACT surfactant, we performed quantum mechanical (QM) calculations of the model esterolytic reaction on the ACT headgroup. The rate-determining step of this process was determined to be the formation of a charged quaternary intermediate, where the ACT becomes covalently attached to the carbonyl carbon of PNB following an initial nucleophilic attack (fig. S3). The formation of a similar enzyme-substrate quaternary transition state also constitutes the rate-determining step during enzymatic catalysis (*55*). To determine the ACT functional group that undertakes substrate attack, we modeled the Gibbs free energy of activation of the addition reaction for the three strongest nucleophilic groups present on the ACT (i.e., the hydroxyl, the tertiary amine, and the imidazole) (Fig. 2C). Under the assay conditions, the lowest energy transition state was observed for the ACT-substrate complex formed via attack by the hydroxyl group (+67.2 kJ mol^{-1}), again similar to the mechanism of the native enzyme. Furthermore, for this transition state to be established, the imidazole group must be located nearby to accept the hydroxyl-H upon the addition to the carbonyl of PNB. Frequency analysis of this transition state confirms a bimodal frequency, corresponding to the O→C addition with a concomitant H→N transfer. All calculations performed on geometries that did not have the hydroxyl and imidazole groups next to each other failed to find a transition-state structure, offering support for a concerted action between the hydroxyl and imidazolyl groups to affect catalysis.

Hydrophobic pocket

A key design feature of the ACT-surfactant system is the development of an internal hydrophobic region via micelle self-assembly. In addition, the formation of micelles may serve additional roles in catalysis, including drawing multiple functional groups together and tuning their reactivity, as well as attracting and partitioning lipophilic substrates (*29*). Inspired by previous reports of enhanced hydrolytic catalysis in a low-polarity environment, we sought to investigate the effect of micelle aggregation on the interaction and catalytic activity of the ACT (*56*, *57*).

The functional group interactions of the ACT appear to be tuned by the inclusion of the ACT surfactant into a co-micelle system with CTAB when analyzed by one-dimensional (1D) and 2D ^{1}H nuclear magnetic resonance (NMR) (Fig. 3, A and B). Analysis of ACT-C_8

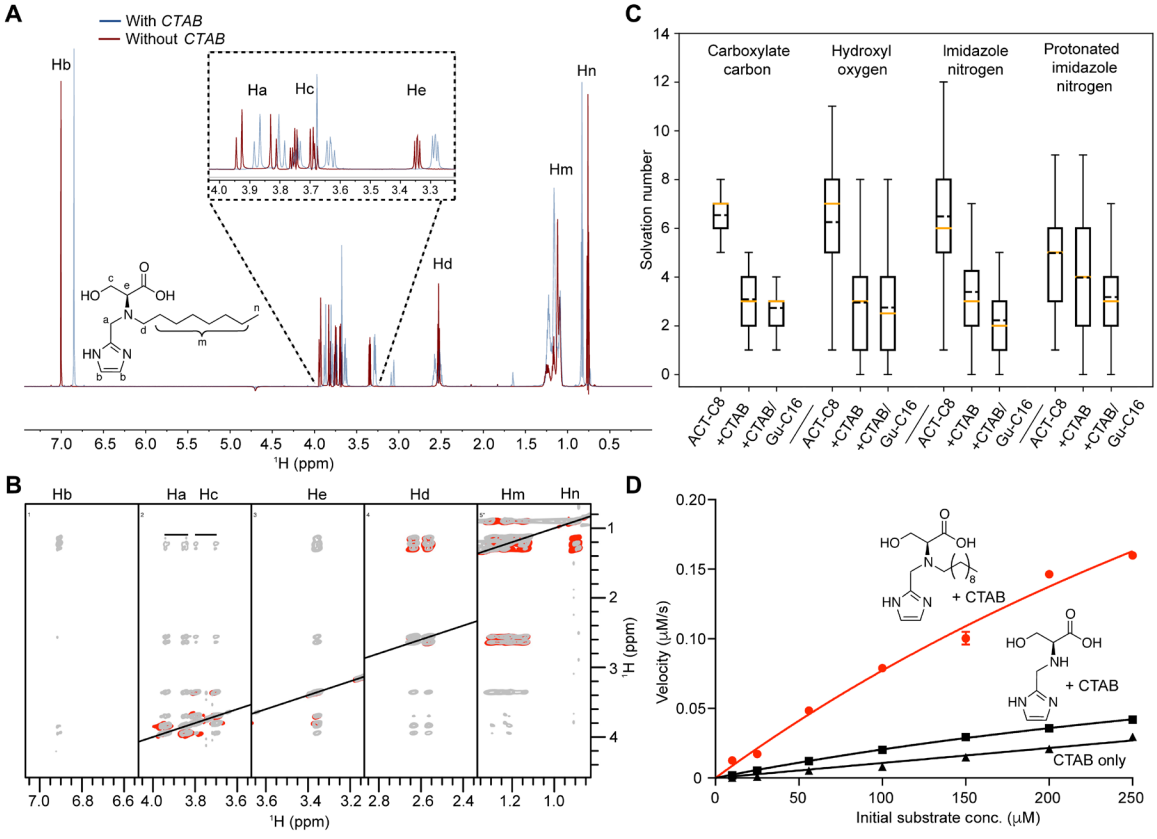

Fig. 3. Mimicking the hydrophobic pocket. (**A**) Analysis of the eight-carbon ACT surfactant via ^{1}H NMR reveals changes to the ACT proton environment in the presence (blue line) and the absence (red line) of *d*-CTAB micelles. (**B**) Five hundred–millisecond ^{1}H NOESY (gray) and 100-ms TOCSY (red) 2D spectra of ACT-C_8 in the presence of *d*-CTAB micelles. Strong through-space interactions between Hb and Hm and the absence of interaction between Hb and He/Hc indicate a preferential orientation of the imidazole ring toward the hydrophobic core of the micelle. (**C**) Solvation number of key ACT-C_8 functional groups predicted by MD simulation, in the absence of cosurfactants (ACT-C_8), upon the addition of CTAB (+CTAB), and upon the addition of both surfactants (+CTAB and Guan-C_{16}). The average number of water molecules surrounding each functional group decreased reliably upon the addition of surfactant and cosurfactant, indicating an increasingly hydrophobic environment. (**D**) Michaelis-Menten kinetics profile of PNB esterolysis catalyzed by the ACT-C_8 surfactant, ACT (nonsurfactant), or CTAB only. An increased catalytic effect was observed when incorporating amphiphilic character into the ACT structure by enhancing interaction with CTAB micelles. [Assay conditions: 25°C; 0.1 M borate buffer (pH 9.0), [catalyst] = 2.24 μM; [CTAB] = 0.8 mM; [substrate] = 10 to 250 μM.] (Data points are the mean of at least three independent experiments, and error bars represent SEM.)

both with and without the addition of deuterated CTAB (*d*-CTAB) (0.8 mM) highlights a significant change in ^{1}H chemical shift in the presence of *d*-CTAB micelles, indicating insertion of the ACT surfactant into the micelle. The most significant shift was observed for the imidazole ring protons (Hb; see Fig. 3A for annotations), 0.15 parts per million (ppm) upfield compared with the CTAB-free system, which may be due to an orientation of these protons into a more hydrophobic environment, such as the core of the *d*-CTAB micelle. This is supported by total correlation spectroscopy (TOCSY) and nuclear Overhauser effect spectroscopy (NOESY) spectra, which confirm strong through-space interactions between Hb and the acyl chain protons (Hm) of the surfactant tail (Fig. 3B). Weak through-space interactions were also observed between Hb and the imidazolyl-adjacent methylene protons (Ha) and between Hb and the closest acyl protons (Hd), which is expected considering the proximity imposed by the compound chemical structure. With the lack of interaction between Hb and the hydroxyl-adjacent methylenes (Hc), it is likely that the imidazole ring is buried into the micelle while the hydroxyl group is facing away toward the aqueous solution. This is further supported by the weaker through-space interactions between Hc and Hd or Hm. The NOESY/TOCSY results indicate some interaction between all three ACT functional groups as well as between the ACT groups and the surfactant alkyl chain.

The incorporation of ACT surfactant into the CTAB micelle was also suggested by molecular dynamics (MD) simulation. Upon incorporation into the micelle, MD simulation highlighted a marked decrease in the number of water molecules surrounding each of the key functional groups the ACT-C_8 surfactant (Fig. 3C). This effect was enhanced for the ACT-C_{16} surfactant, whose longer alkyl chain resulted in a deeper incorporation into the micellar assembly. In the absence of CTAB, the ACT surfactants were not observed to form persistent aggregates over 100 ns of simulation, suggesting that the ACT is only incorporated into a hydrophobic environment in the presence of cosurfactants (fig. S4). Also observed were changes to the interactions between functional groups of the ACT surfactants upon incorporation into the micelle (figs. S11 and S12). The intramolecular distance between functional groups of the ACT was altered following micelle assembly, establishing closer interactions between the imidazole ring and the carboxylate and hydroxyl moieties of the ACT, consistent with experimental NOESY data (vide supra). In addition, micelle incorporation resulted in a substantial shift in the separation distribution between the hydroxyl group and the imidazole

ring toward shorter-range interactions. Combined with the available solvation and NMR data, this suggests a significant contribution by the micelle self-assembly process to tune the electrostatic interactions and local nano-environment of the ACT functional groups.

To examine the impact of ACT-surfactant self-assembly on catalysis, we also assayed the ACT headgroup (without an alkyl chain) for PNB esterolysis (Fig. 3D). The ACT molecule displays excellent water solubility in isolation, and it is likely that this material would be poorly incorporated into a micellar assembly. A significant reduction in catalysis was observed for the ACT molecule compared with the ACT-C_8 surfactant, when assessed in combination with CTAB. This result provides insight into the environmental effects, which help to facilitate catalysis, whereby positioning of the ACT close to the hydrophobic PNB substrate is achieved through the addition of surfactant functionality to the ACT and subsequent self-assembly. Without surfactant functionality, the ACT unit is likely to be distributed broadly in solution, limiting the kinetics of substrate interaction and catalysis. In addition, a reduced catalytic effect was observed when moving from a longer alkyl chain surfactant ACT-C_{16} to the shorter alkyl chain ACT-C_8, further emphasizing the effect of catalyst environment. These assay findings offer support to both the computational and NMR results, highlighting the impact of localizing the ACT into a micelle environment for tuning functional group interactions and enhancing catalysis.

H-bond cosurfactant

While the active site and hydrophobic pocket are essential functional components in enzymatic reactions, stabilization of transition states via H-bonding is a key stage common in biocatalysis. We proposed that the localization of a strongly H-bond donating group (i.e., guanidinium) nearby to the ACT headgroup within a micelle assembly may assist catalysis, similar to the role of the oxyanion hole in α-chymotrypsin. Excluding the Gu-C_{16} from the cosurfactant system resulted in an approximately fourfold decrease in catalytic activity, highlighting the strong contribution of Gu-C_{16} to effect catalysis (Fig. 4D). Examination of the cosurfactant system containing only

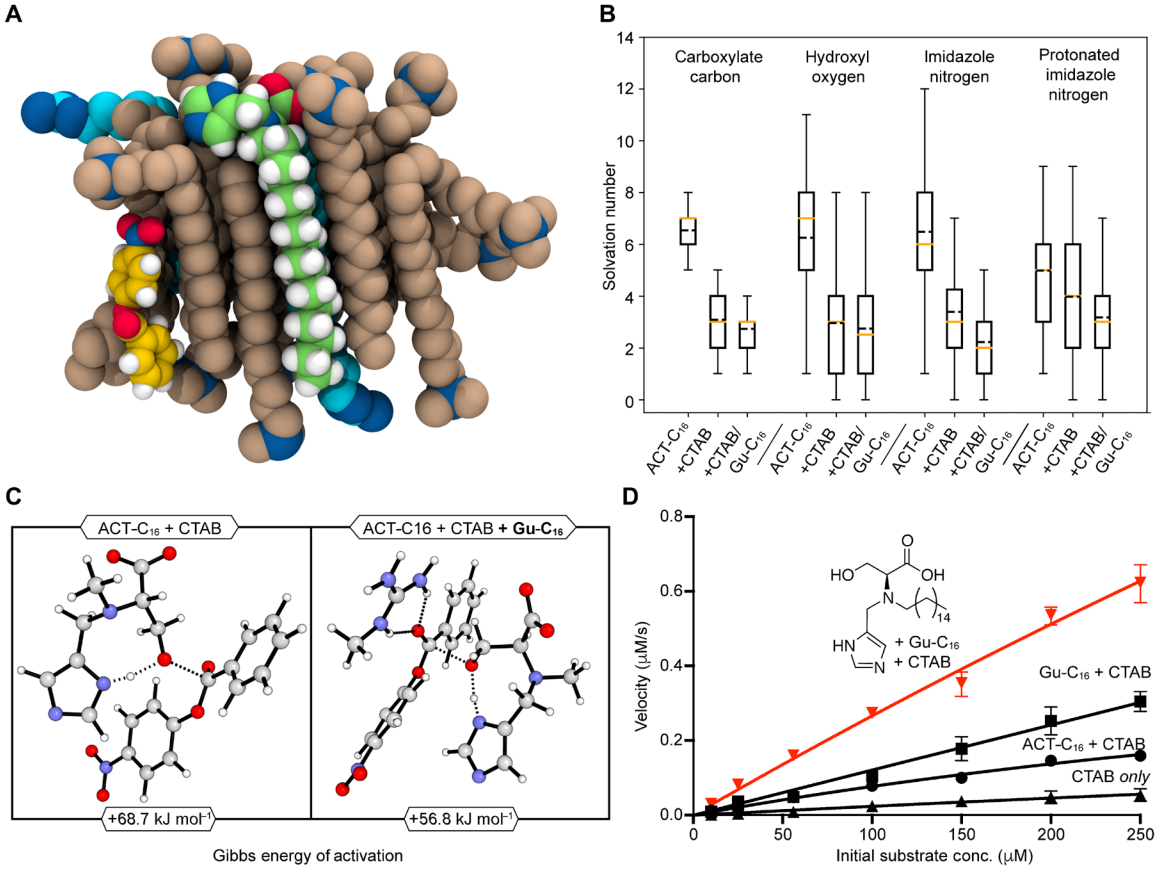

Fig. 4. Enhancing catalysis by incorporating a guanidine-based surfactant. (**A**) Cross section of a representative micelle observed via MD simulation, highlighting both catalyst and substrate incorporated into the hydrophobic core following aggregation of CTAB and Guan-C_{16} cosurfactants. The catalytic groups of ACT-C_{16} (lime green) are largely buried in the micelle environment. CTAB and Guan-C_{16} molecules are shown in tan and cyan van der Waals representation, respectively, with hydrogen atoms omitted for clarity. PNB is shown in yellow. Nitrogen atoms are shown in dark blue, and oxygen atoms are shown red. (**B**) Solvation number of the ACT-C_{16} polar functional groups predicted by MD simulation, in the absence of cosurfactants (ACT-C_{16}), upon the addition of CTAB (+CTAB), and upon the addition of both surfactants (+CTAB and Guan-C_{16}). The average number of water molecules surrounding each functional group was markedly decreased upon the addition of both cosurfactants, indicating enhanced incorporation of ACT-C_{16} into the hydrophobic micelle core. (**C**) QM simulation of the model esterolysis reaction revealed a decrease in Gibbs activation energy of 11.9 kJ mol^{-1} when Guan-C_{16} is incorporated into the cosurfactant system. This corresponds to an approximately two orders of magnitude increase in the rate of substrate addition to ACT-C_{16} (rate-determining step). (**D**) Michaelis-Menten kinetics profile of PNB esterolysis catalyzed by ACT-C_{16} in a cosurfactant system with CTAB and Guan-C_{16}. Incorporation of all three cosurfactants into the catalyst assembly resulted in enhanced catalysis compared with the single- or two-component systems. (Data points are the mean of at least three independent experiments, and error bars represent SEM.)

Gu-C_{16} and CTAB revealed a higher catalytic effect than for the ACT-C_{16}/CTAB system. This may be due to the higher concentration of Gu-C_{16} used in the assay compared with ACT-C_{16} (0.3 mM versus 0.002 mM, respectively) and indicates that the guanidinium surfactant by itself is also capable of facilitating hydrolysis, potentially via combined general base catalysis and induced micellar catalysis at the charged assembly interface. The strong, bifurcated H-bond donation of guanidinium could also serve to activate the carbonyl to attack by alternative nucleophilic species in solution; such has been reported in ring-opening polymerizations (*40*, *58*). Despite this, the highest rate enhancement was observed for the three-component system, which gives support for the concerted action of the guanidinium and ACT headgroups in catalysis. Although other Lewis acid structures may perform similar tasks, we believe that the guanidinium headgroup offers benefits, such as facile synthesis, double H-bond donation, and a high pKa.

To further probe the cooperation between the ACT and guanidinium surfactants, we conducted computational modeling on the co-micelle assembly and catalytic mechanism. Assessment via MD simulation revealed the aggregation of Guan-C_{16} with CTAB, ACT surfactant, and PNB substrate into a co-micellar assembly, whose size, morphology, and composition are consistent with previous literature (Fig. 4A and figs. S4 to S6) (*59*). The average aggregation number of the micelles was observed to increase upon the addition of the Guan-C_{16} cosurfactant, which may be a result of increased availability of surfactants, rather than insufficient simulation time. In all cases, the composition of the assembly following the addition of Guan-C_{16} affected the solvation of the key ACT functional groups, with consistently increased solvation numbers pointing toward a deeper inclusion of the ACT into the micellar aggregate (Fig. 4B). This effect may also be a result of charge-screening effects afforded to the catalyst by the cationic Gu-C_{16} headgroup, potentially illustrating electrostatic contact between the ACT and guanidinium units. In contrast, no preferential interaction between the guanidinium group and the acyl group of the PNB substrate was observed during simulation, although this does not preclude the possibility of catalytically relevant transition-state stabilization interactions between the two groups. Rather, this may suggest that the additional rate enhancement afforded by Gu-C_{16} may arise from an electronic interaction with the ACT, as well as physically allowing the catalyst to bury further into the micelle environment.

To provide deeper insight into the origin of the increased rate enhancement on the addition of Gu-C_{16} to the co-micelle system, we introduced a positively charged guanidinium headgroup to the QM calculations of the model assay reaction. Subtle changes to the rate-determining transition-state structures were observed when the guanidinium headgroup is positioned proximate to the acyl group of the PNB substrate (Fig. 4C). More specifically, the guanidinium unit formed a bifurcated H-bond with the carbonyl oxygen of PNB, withdrawing electron density from the scissile carbon and lowering the barrier for nucleophilic attack by the ACT. As a result, the Gibbs energy of the rate-determining intermediate was reduced by −11.9 kJ mol^{-1}, which corresponds to an approximately two orders of magnitude increase in the rate of ACT→PNB addition. This result reflects the enhanced catalysis observed experimentally on the addition of Gu-C_{16} to the co-micellar assembly. Because of a lack of rigidity in the micelle structure and the dynamic nature of headgroup interactions, this remarkable rate enhancement is not fully reflected in the experimental assay results. However, there is clear potential for a supporting H-bond donor to complement the catalysis of the ACT, and further study exploring optimal group arrangements is ongoing.

CONCLUSION

In summary, we report the development of a bioinspired cosurfactant micelle system that undertakes hydrolysis of a model ester substrate via a proposed mechanism similar to native enzymes. Drawing inspiration from the catalytic triad, oxyanion hole, and hydrophobic binding pocket common to many hydrolases, the co-micelle assembly collects multiple functional groups into close proximity around a macromolecular capsule to affect catalysis. Structural assessment via XRD, ^{1}H NMR, and 2D ^{1}H NMR supports the close interaction of the three groups of the ACT, as well as highlighting the importance of surfactant functionality for optimizing the local nano-environment. Furthermore, computational modeling via QM calculations and MD simulation further support the close relationship between functional groups in the co-micelle catalyst and the notable similarity of the catalytic mechanism to native enzymatic reactions. Highly functional surfactants hold promise for the future design of multifunctional, enzyme-inspired catalysts, although much work remains to be done before we may realize a true model of these incredibly complex natural proteins.

MATERIALS AND METHODS

General information

All commercially obtained solvents and reagents were used without further purification. Analytical thin-layer chromatography was carried out on Merck silica gel 60 F_{254} glass plates, and flash chromatography was performed on Merck silica gel 60 (70 to 230 mesh).

Visualization was accomplished with short-wave ultraviolet (UV) light and/or $KMnO_4$ staining solution followed by gentle heating. Surfactants were purified by preparative reverse-phase high-performance liquid chromatography (RP-HPLC) on a Biotage SP1 HPFC Flash Purification System using a reverse-phase Biotage SNAP Cartridge (KP-C18-HS, 60 g). For synthesis characterization, ^{1}H and ^{13}C solution-state NMR were recorded on a Varian Unity Inova 500 (500 MHz for ^{1}H and 125 MHz for ^{13}C) or a Varian Unity Inova AS600 (600 MHz for ^{1}H and 150 MHz for ^{13}C) spectrometer. Chemical shifts δ are reported relative to the resonance signal of ^{1}H or ^{13}C cores of tetramethylsilane and in parts per million. The ^{1}H spectra were calibrated by setting the solvent peaks, caused by remaining traces of protons, to values known from the literature ($\delta CHCl_3$ = 7.26 ppm, δCD_3OH = 4.87 ppm, and δD_2O = 4.79 ppm). The coupling constants *J* are reported in hertz.

CMC measurements—Pyrene method

According to the literature (*60*), a pyrene stock solution was prepared by dissolving pyrene (5 mg) in methanol (10 ml) and diluting 20-fold with methanol. Pyrene was stored under an inert atmosphere at 4°C, and stock solutions were prepared fresh each day. Surfactant stock solutions (~0.1 M) were prepared in dimethyl sulfoxide (DMSO) or borate (pH 9.0) ($Na_2B_4O_7{\cdot}10H_2O$) buffer according to the individual surfactant solubilities. For the fluorescence assay, an appropriate volume of surfactant stock solution (surfactant final concentration range, 0.01 to 0.8 mM) was transferred to a quartz fluorescence cuvette. Pyrene stock solution (50 μl) and either deionized water or borate buffer (pH 9.0) were added to the cuvette for a final volume

of 2.5 ml. In the cases where the surfactant was dissolved in DMSO, a small aliquot of DMSO was added to the cuvette to maintain a constant DMSO concentration for all surfactant concentrations [final DMSO concentration, <1% (v/v)]. The fluorescence emission spectrum of pyrene was measured immediately after mixing using an emission wavelength scanning mode from 360 to 400 nm over 90 s. The excitation wavelength was 334 nm (slit width, 8 nm), and emission slit width was 2 nm. The first and third fluorescent vibrational peaks (I_1 and I_3) were recorded at 373 and 384 nm, respectively, and the ratio was plotted against surfactant concentration for the CMC calculations. The midpoint of the inflection of I_1/I_3 versus surfactant concentration was taken as the CMC value in all cases (fig. S1).

Esterolysis assay with *p*-nitrophenyl benzoate (representative assay for the three-component catalyst)

Catalyst (ACT surfactant, 2.24 μM) was dissolved with cetyl ammonium bromide (CTAB; 0.8 mM) and hexadecylguanidinium chloride (Gu-C_{16}; 0.3 mM) in a borate ($Na_2B_4O_7{\cdot}10H_2O$) buffer at pH 9 (c_{buffer} = 100 mM) with vigorous stirring. Control reactions lacking either CTAB, ACT surfactant, or Gu-C_{16} were also conducted with the same concentrations. A stock solution of substrate *p*-nitrophenyl benzoate was made up in acetonitrile and added to the buffered solution containing surfactants ($c_{substrate,initial}$ = 10, 25, 56, 100, 150, and 250 μM). A small aliquot of acetonitrile was added to the reference cell to maintain consistency [acetonitrile concentration, <5% (v/v)]. Following mixing, the reaction was immediately monitored via UV light absorption at 405 nm at room temperature in a Cary 60 UV-visible spectrophotometer (Agilent). The kinetics of ester substrate consumption was calculated via nonlinear regression using the plotting software GraphPad Prism 8, under an assumption of Michaelis-Menten kinetics. The background hydrolysis rate without the addition of catalyst or surfactants was determined using a first-order rate assumption, where k_{cat} is equal to the $k_{hydrolysis}$ for the reaction.

For the enzyme-catalyzed control reaction, α-chymotrypsin (from bovine pancreas type II, lyophilized powder, Sigma-Aldrich) (2.2 μM) was dissolved as received in borate ($Na_2B_4O_7{\cdot}10H_2O$) buffer at pH 9 (c_{buffer} = 100 mM), containing CTAB (0.8 mM). A stock solution of substrate *p*-nitrophenyl benzoate was made up in acetonitrile and added to the buffered solution containing surfactants ($c_{substrate,initial}$ = 10, 25, 56, 100, 150, and 250 μM), as per the surfactant experiments above. The hydrolysis reaction was assessed over 10 min and compared directly with the results of the cosurfactant systems.

X-ray crystallography of ACT-C_8 surfactant

The crystal data of the ACT-C8 surfactant were collected on a charge-coupled device diffractometer using Cu-Kα radiation (graphite crystal monochromator = 1.54184 Å). The structure was solved by direct methods (SHELXT) and difference Fourier synthesis. Thermal ellipsoid plots were generated using the program ORTEP-3 integrated within the WinGX suite of programs. $C_{15}H_{27}N_3O_3$: M = 297.39, T = 130.0(2) K, λ = 1.54184 Å; monoclinic, space group $P2_1$: a = 12.9624(5), b = 8.4191(3), c = 14.9957(6) Å, β = 93.510(3), V = 1633.44(11) Å^3, Z = 4, Z' = 2, D_c = 1.209 Mg M^{-3} μ(Cu-Kα) = 0.685 mm^{-1}, F(000) = 648; crystal size, 0.65 mm by 0.21 mm by 0.03 mm. θ_{max} = 76.48, 9264 reflections measured, 4774 independent reflections (R_{int} = 0.058), the final R = 0.0567 [I > 2σ(I), 4459 data], and $wR(F^2)$ = 0.1559 (all data) Goodness-of-fit = 1.073, absolute structure parameter 0.0(2). Cambridge Crystallographic Data Centre code: 1900732.

NMR of ACT-C_8 surfactant

NMR samples were prepared by either dissolving ACT-C8 in buffer [50 mM borate (pH 9.0), 0.05 mM DSS (4,4-dimethyl-4-silapentane-1-sulfonic acid), 10% (v/v) D_2O] or in 75 mM deuterated CTAB [50 mM borate (pH 9.0), 0.05 mM DSS, 10% (v/v) D_2O] to reach a final compound concentration of ca. 5 mM. NMR spectra were obtained at 298 K on an 800-MHz Bruker Avance II equipped with a TCI CryoProbe. Chemical shifts were referenced to DSS at 0 ppm. Data were processed in TopSpin (Bruker) and analyzed using the CCPNmr Analysis program (Laue 2005 Proteins 59, 687). ^{1}H homonuclear correlation spectroscopy, TOCSY (mixing time τ_{mix} = 100 ms), and NOESY (τ_{mix} = 100 and 500 ms) were run using 4000 and 512 points in the direct and indirect dimensions, respectively.

Synthetic procedures

Reductive amination of L-serine with 1H-imidazole-2-carboxaldehyde (preparation of ACT molecule)

L-Serine (1.05 g, 10 mmol, 1.00 eq) and sodium hydroxide (420 mg, 10.5 mmol, 1.05 eq) were dissolved in methanol ($c_{L\text{-serine}} \approx$ 85 mM), and 1*H*-imidazole-2-carboxaldehyde or 1*H*-imidazole-4-carboxaldehyde (1.06 g, 11 mmol, 1.10 eq) was added to the solution with stirring. The mixture was stirred at 40°C for 30 min and afterward allowed to cool down to room temperature over 4 hours while stirring. Sodium borohydride (605.3 mg, 16 mmol, 1.60 eq) was added slowly, and the reaction mixture was stirred at room temperature for 30 min. Glacial acetic acid was added dropwise until the mixture reached approximately pH 4 to 5, and the resulting suspension was stirred at room temperature for a further 10 min. The product was obtained as the precipitate by filtration and washing with methanol. ACT was collected as a fine, white solid (yield 99%).

[ACT (2-imidazole isomer)] ^{1}H NMR (600 MHz; D_2O, 298 K): δ = 7.23 (*s*, 2H, aromatic), 4.31 (*d*, ^2J = 15.1 Hz, 1H, C*H*HN), 4.23 (*d*, ^2J = 15.1 Hz, 1H, CH*H*N), 3.95 to 3.77 (*m*, 2H, CH_2OH), 3.56 (dd, ^3J = 5.3 Hz, ^3J = 4.1 Hz, 1H, CHCO$_2^-$). MS [electrospray ionization (ESI)] was calculated for $C_7H_{11}N_3O_3H^+$ ([M + H]$^+$): 186.09. Found: 186.09.

[ACT (4-imidazole isomer)] ^{1}H NMR (400 MHz, CD_3OD, 298 K): δ = 7.66 (s, 1H, Im), 7.17 (s, 1H, Im), 4.15 (d, J = 13.9 Hz, 1H, CH_2OH), 4.11 (d, J = 13.9 Hz, 1H, CH_2OH), 3.84 (dd, J = 12.9, 3.9 Hz, 1H, CH_2Im), 3.78 (dd, J = 12.9, 3.9 Hz, 1H, CH_2Im), 3.57(*t*, J = 7.4, 3.8 Hz, 1H, C*H*CH$_2$OH). MS (ESI) was calculated for $C_7H_{11}N_3O_3H^+$ ([M + H]$^+$): 186.09. Found: 186.09.

Preparation of *n*-octan-1-al from *n*-octan-1-ol

According to the literature (*61*), *n*-Octan-1-ol (1.3 g, 10 mmol, 1.0 eq) was dissolved in dichloromethane ($c_{alcohol} \approx$ 65 mM), and pyridinium dichromate (4.5 g, 12 mmol, 1.2 eq) was added to the solution portionwise. The mixture was stirred at room temperature for 8 hours. The suspension was filtered through filter paper and a short silica pad. The solid residue was washed several times with diethyl ether. The solvents were removed in vacuo, and the crude product was purified by flash chromatography (hexane/ethyl acetate = 19:1) to yield a waxy colorless solid (819 mg, 64%). ^{1}H NMR (400 MHz, $CDCl_3$, 298 K): δ = 9.74 (t, J = 1.9 Hz, 1H, C*H*O), 2.40 (td, J = 7.4, 1.9 Hz, 2H, CH_2CHO), 1.60 (m, CH_2, 2H), 1.35 to 1.19 (m, CH_2, 8H), 0.86 (t, J = 6.8 Hz, 3H).

Preparation of *n*-hexadecan-1-al from *n*-hexadecan-1-ol

1-Hexadecanol (5.00 g, 20.6 mmol, 1.00 eq) was dissolved with stirring in dichloromethane (150 ml). Pyridinium dichromate (9.40 g,

25.0 mmol, 1.20 eq) was added portionwise, and the mixture was stirred for a further 5 hours. The suspension was filtered over a short silica pad and washed several times with dichloromethane and ethyl acetate, and the filtrate was dried in vacuo. Purification of the crude product by column chromatography (hexane/ethyl acetate = 19:1) yielded target aldehyde as a colorless solid (3.69 g, 15.3 mmol, 74%). ^{1}H NMR (500 MHz, $CDCl_3$, 298 K): δ = 9.76 (t, ^3J = 1.9 Hz, 1H, C*H*O), 2.41 (td, ^3J = 7.4 Hz, ^3J = 1.9 Hz, 2H, CH_2CHO), 1.66 to 1.58 (m, 2H, CH_2), 1.35 to 1.21 (m, 24H, CH_2), 0.88 (t, ^3J = 6.9 Hz, 3H, CH_3).

Reductive amination of ACT with *n*-octan-1-al (preparation of ACT-C_8 surfactant)

The corresponding ACT (1.00 eq) and sodium hydroxide (1.05 eq) were dissolved in methanol ($c_{precursor}$ ≈ 100 mM). *n*-Octan-1-al (1.20 eq) and sodium triacetoxyborohydride (1.40 eq) were added to the solution, and the mixture was stirred at 40°C for 2 hours. Another two batches of *n*-octan-1-al (2 × 1.20 eq) and sodium triacetoxyborohydride (2 × 1.40 eq) were added to the solution every 2 hours, and after 4 hours, the mixture was left to stir at 40°C for a further 20 hours. The reaction was quenched with glacial acetic acid, and the solvents were removed in vacuo. The crude product was washed with ethyl acetate and purified by RP-HPLC with an H_2O/acetonitrile gradient (19:1→1:19). (Both derivatives a pale-yellow solid, 2-isomer = 60%, 4-isomer = 84%.) (ACT-C_8 2-isomer) ^{1}H NMR (500 MHz; D_2O, 298 K): δ = 7.78 (*s*, 1H, Im), 7.32 (*s*, 1H, Im), 4.34 to 4.18 (*m*, 2H, ImCH_2N), 4.00 to 3.82 (*m*, 2H, CH_2OH), 3.57 (dd, ^3J = 6.9 Hz, ^3J = 5.2 Hz, 1H, C*H*CO_2H), 2.86 to 2.70 (*m*, 2H, CH_2CH_2N), 1.44 to 1.30 (*m*, 2H, CH_2CH_2N), 1.24 to 1.03 (m, 10H, CH_2), 0.75 (*t*, ^3J = 6.8 Hz, 3H, CH_3). MS (ESI) was calculated for $C_{15}H_{27}N_3O_3H^+$ ($[M + H]^+$): 298.21. Found: 298.24.

Reductive amination of ACT with *n*-hexadecan-1-al (preparation of ACT-C_{16} surfactant)

The corresponding ACT (185 mg, 1.0 mmol, 1.00 eq) was dissolved in methanol and glacial acetic acid ($c_{amino\ acid\ precursor}$ ≈ 12.3 M) with stirring at 60°C. C_{16} aldehyde (360 mg, 1.5 mmol, 1.50 eq) was added, and the reaction was mixed for 20 min. Sodium triacetoxyborohydride (420 mg, 2.0 mmol, 2.0 eq) was added carefully to the solution, and stirring was continued at 60°C for 4 hours. Another batch of aldehyde (360 mg, 1.5 mmol, 1.50 eq) and Sodium triacetoxyborohydride (420 mg, 2.0 mmol, 2.0 eq) was added, and the mixture was stirred at 60°C for a further 24 hours. The reaction was quenched with water, and the solvents were removed in vacuo at elevated temperature. The crude product was extracted with methanol and washed several times with ethyl acetate before being purified by reverse-phase column chromatography (H_2O/methanol = 19:1→1:19→0:1) to yield ACT-C_{16} surfactant (213 mg, 0.52 mmol, 52%). ^{1}H NMR (400 MHz, CD_3OD, 298 K): δ = 7.77 (s, 1H, Im); 7.35 (s, 1H, Im); 4.51 (d, *J* = 13.9 Hz, 1H, CH_2OH); 4.42 (d, *J* = 13.9 Hz, 1H, CH_2OH), 4.17 (dd, *J* = 12.9, 3.9 Hz, 1H, CH_2Im), 4.05 (dd, *J* = 12.9, 3.9 Hz, 1H, CH_2Im); 3.82 (dd, *J* = 7.4, 3.8 Hz, 1H, C*H*CH_2OH); 2.24 (t, *J* = 7.4 Hz, 1H, CH_2N); 1.57 (p, *J* = 7.2 Hz, 2H, CH_2CH_2N); 1.40 to 1.22 (m, 26H, CH_2); 0.88 (t, J = 7.2 Hz, 3H, CH_3). MS (ESI) was calculated for $C_{23}H_{43}N_3O_3H^+$ ($[M + H]^+$): 410.33. Found: 410.34.

1-Hexadecylguanidinium chloride (Gu-C_{16})

According to the literature (*43*), 1-hexadecylamine (723 mg, 3.0 mmol, 1.0 eq) was dissolved in methanol (15 ml) at 40°C with stirring. 1H-pyrazole-1-carboxamidine hydrochloride (438 mg, 3.0 mmol, 1.0 eq) was added, and stirring was continued at 40°C for 3 days. Solvent was removed in vacuo, and the crude product was washed three times with hot acetone to yield target surfactant **Gu-C_{16}** as a colorless solid (850 mg, 2.9 mmol, 97%). ^{1}H NMR (400 MHz, CD_3OD, 298 K): δ = 3.14 (*t*, *J* = 7.1 Hz, 2H), 1.56 (*p*, *J* = 7.2 Hz, 2H), 1.41 to 1.22 (*m*, 26H), 0.87 (*m*, 3H). MS (ESI) was calculated for $C_{17}H_{33}N_3H^+$ ($[M + H]^+$): 284.30. Found: 284.32.

Preparation of (OH–COOH) control structure [(*S*)-3-hydroxy-2-(octylamino)propanoic acid]

L-serine (210 mg, 2.0 mmol, 1.0 eq) was suspended in 15 ml of methanol at 50°C, and sodium hydroxide (88 mg, 1.4 mmol, 1.1 eq) was added with stirring. 1-Octanal (310 mg, 2.4 mmol, 1.2 eq) was then added, and the reaction was mixed overnight at room temperature. $NaBH_4$ (150 mg, 4.0 mmol, 2.0 eq) was then added, and the reaction mixture was stirred for a further 1 hour at room temperature. Concentrated hydrochloric acid (32%, ~0.7 ml) was added to quench the reaction mixture, the suspension was filtered, and solvent was removed in vacuo. The crude product was washed with ethyl acetate and then purified via reverse-phase column chromatography (MeOH/H_2O 19:1→0:1) to yield target structure (239 mg, 1.1 mmol, 54%). ^{1}H NMR (400 MHz; CD_3OD, 298 K): δ = 3.93 (dd, *J* = 11.8, 4.0 Hz, 2H, CH_2OH), 3.82 (dd, *J* = 11.8, 6.4 Hz, 2H, CH_2OH), 3.46 (dd, *J* = 6.4, 4.0 Hz, 1H, C*H*CH_2OH), 2.95 (*m*, 2H, CH_2NH), 1.67 (*p*, *J* = 7.6 Hz, 2H), 1.38 to 1.13 (*m*, 10H, CH_2), 0.97 to 0.80 (m, 3H, CH_3). MS (ESI) was calculated for $C_{11}H_{23}NO_3H^+$ ($[M + H]^+$): 218.17. Found: 218.19.

Preparation of (Im–COOH) control structure [(*R*)-3-(1*H*-imidazol-5-yl)-2-(octylamino)propanoic acid]

L-histidine (620.8 mg, 4.0 mmol, 1.0 eq) was suspended in 20 ml of methanol at 50°C, and sodium hydroxide (168 mg, 4.2 mmol, 1.1 eq) was added with stirring. 1-Octanal (620 mg, 4.8 mmol, 1.2 eq) was then added, and the reaction was mixed overnight at room temperature. $NaBH_4$ (300 mg, 8.0 mmol, 2.0 eq) was then added, and the reaction mixture was stirred for a further 1 hour at room temperature. Concentrated hydrochloric acid (32%, ~1.0 ml) was added to quench the reaction mixture, the suspension was filtered, and the solvent was removed in vacuo. The crude product was washed with ethyl acetate and a small volume of water and then purified via reverse-phase column chromatography (MeOH/H_2O 19:1→0:1) to yield target structure (639 mg, 2.4 mmol, 60%). ^{1}H NMR (400 MHz; CD_3OD, 298 K): δ = 8.74 (s, 1H, Im); 7.38 (s, 1H, Im); 3.71 to 3.60 (m, 1H, C*H*COOH), 3.54 to 3.43 (m, 2H, CH_2Im), 3.08 to 2.97 (m, 2H, CH_2NH), 1.47 to 1.35 (m, 2H, CH_2CH_2NH), 1.31 to 1.07 (*m*, 10H, CH_2); 0.79 to 0.7 (m, 3H, CH_3). MS (ESI) was calculated for $C_{14}H_{25}N_3O_2H^+$ ($[M + H]^+$): 268.20. Found: 268.21.

Preparation of (Im–OH) control structure [(*R*)-3-(1*H*-imidazol-5-yl)-2-(octylamino)propan-1-ol]

L-histidinol dihydrochloride (430 mg, 2.0 mmol, 1.0 eq) was suspended in 15 ml of methanol at 50°C, and sodium hydroxide (180 mg, 4.2 mmol, 2.1 eq) was added with stirring. The cloudy suspension was filtered, 1-octanal (260 mg, 2.1 mmol, 1.05 eq) was then added, and the reaction was mixed overnight at room temperature. $NaBH_4$ (90 mg, 2.4 mmol, 1.2 eq) was then added, and the reaction mixture was stirred for a further 1 hour at room temperature. Concentrated hydrochloric acid (~0.6 ml) was added to quench the reaction mixture, the suspension was filtered, and the solvent was removed in

vacuo. The crude product was washed several times with ethyl acetate, extracted into methanol, and purified via reverse-phase column chromatography ($MeOH/H_2O$ 19:1→0:1) to yield target structure (214 mg, 0.8 mmol, 42%). ^1H NMR (400 MHz; CD_3OD, 298 K): δ = 8.81 (s, 1H, Im); 7.43 (s, 1H, Im); 4.40 to 4.34 (*m*, 2H, CH_2OH), 4.18 to 4.07 (*m*, 2H, CH_2Im); 3.42 (dd, *J* = 7.4, 3.8 Hz, 1H, $CHCH_2OH$); 3.11 to 2.97 (*m*, 2H, CH_2CH_2N); 2.23 to 2.06 (*m*, 2H, CH_2CH_2N); 1.39 to 1.10 (m, 26H, CH_2); 0.80 (t, *J* = 7.2 Hz, 3H, CH_3). $C_{14}H_{26}N_3O^-$ ($[M - H]^-$): 252.22. Found: 252.21.

Computational procedures

Quantum mechanics

All electronic structure calculations were performed with the Gaussian 16, Revision A.03 (*62*) software package. All density functional theory calculations were performed using the M06-2X functional (*63*) in conjunction with the 6-31+G(d,p) basis set. Implicit solvent effects for all calculations performed were obtained using the SMD (solvent model density) (*64*) solvation model for water. The ACT molecules were truncated by replacement of the extended alkyl chains with a single methyl group and conformationally searched to locate the global minimum energy structure; guanidine was also truncated by replacement of the extended alkyl chain with a single methyl group, so as to determine the possible role of the positively charged headgroup. All entropies, zero-point vibrational energies, and thermal corrections were scaled by recommended scale factors (*65*); vibrational analysis was performed on all geometries to confirm (i) the absence of imaginary frequencies for minimum energy structures and (ii) the presence of a single imaginary frequency for transition-state structures.

Molecular dynamics

MD simulations were performed using the GROMACS 2018.1 engine with parameters from the GROMOS54a7 force field (*66*, *67*). All-atom parameter sets for each surfactant (CTAB, molid 10929; Gu-C16, molid 306970), uncharged catalyst (ACT-C8, molid 306428; ACT-C16, molid 306429), charged catalyst (ACT-C8, molid 306968; ACT-C16, 306969), and substrate (PNB, molid 9503) corresponding to the predicted ionization states at pH 9 were obtained using the Automated Topology Builder V.2.2 (*68*). To remove any conformational bias from the system setup, triplicate systems were prepared in which molecules of substrate, catalyst, and surfactant were randomly orientated in a cubic dodecahedron box at the relative concentrations used in experimental assays (table S2) and solvated with a 7-nm buffer of explicit simple point-charge water. The concentration of surfactant species was increased 10-fold to facilitate sampling. Ions were added as required to neutralize overall system charge. The initial configuration was relaxed using standard steepest descent minimization using at least 1000 steps before being equilibrated for 10 ns in the isothermal–isobaric (*NpT*) ensemble to stabilize the system density. Each catalytic system (simulations 1 to 20; table S2) was allowed to self-assemble for 100 ns under *NpT*. Single CTAB controls (simulations 21 to 25; table S2) were run at various concentrations under the same conditions for 300 ns each. Periodic boundary conditions were used, and long-range electrostatics were calculated using the particle-mesh Ewald method with a cutoff of 14 Å (*69*). The temperature in all simulations was set to 300 K and controlled via the v-rescale thermostat (*70*); the initial velocities of all particles were randomly generated. Pressure coupling was handled with the Berendsen barostat during equilibration and with the Parrinello-Rahman barostat for dynamics. The LINCS (Linear Constraint Solver) algorithm (*71*) was used to constrain bonds in conjunction with an integration time step of 2 fs. All trajectory images were produced in VMD (visual molecular dynamics) (*72*). All data were visualized using Python.

Aggregation numbers and component ratios

Micelle aggregation numbers and component ratios were calculated using a Python program using MDTraj (*73*) written for this purpose that recursively considers the neighbors of each micelle component within a given cutoff to define an aggregate, until no more neighbors are found. A 3-Å cutoff was used, and all micelle components in the simulation box were found using this scheme. Micelle aggregation numbers reported (figs. S4 and S5) are for a single frame of each replicate after 100 ns, after periodicity was considered. Component ratios are reported as the sample mean across replicates at 100 ns, after combining data from simulations run at different protonation states, in fig. S6.

Hydration number

Hydration numbers were calculated by searching for solvent molecules near a given atom within a cutoff of 4 Å, which was determined to be optimal by generating radial distribution functions (fig. S10) for the solvent surrounding each atom of interest from simulations containing only the catalyst in water. Data reported are the distribution for each simulation over the whole simulation time, as reported in table S2. The hydration numbers of catalytically relevant atoms of interest are given in figs. S7 to S9.

Intramolecular distances

Intramolecular distances between relevant atoms of the catalysts were measured as the Cartesian distance between the groups at each frame of the final trajectory, after considering periodic boundary conditions. The intramolecular distances of each catalyst monomer were considered separately, and the overall distance data reported are the distributions over the total simulation time of each set of replicates (figs. S11 and S12).

SUPPLEMENTARY MATERIALS

Supplementary material for this article is available at http://advances.sciencemag.org/cgi/content/full/6/14/eaaz0404/DC1

REFERENCES AND NOTES

1. A. Warshel, P. K. Sharma, M. Kato, Y. Xiang, H. Liu, M. H. M. Olsson, Electrostatic basis for enzyme catalysis. *Chem. Rev.* **106**, 3210–3235 (2006).
2. J. McMurry, T. P. Begley, *The Organic Chemistry of Biological Pathways* (Roberts and Company Publishers, Englewood, Colorado, USA, 2005).
3. A. J. Kirby, Efficiency of proton transfer catalysis in models and enzymes. *Acc. Chem. Res.* **30**, 290–296 (1997).
4. F. M. Menger, Enzyme reactivity from an organic perspective. *Acc. Chem. Res.* **26**, 206–212 (1993).
5. D. E. Koshland, The key–lock theory and the induced fit theory. *Angew. Chem. Int. Ed. Engl.* **33**, 2375–2378 (1995).
6. A. J. Kirby, Enzyme mechanisms, models, and mimics. *Angew. Chem. Int. Ed. Engl.* **35**, 706–724 (1996).
7. X. Zhang, K. N. Houk, Why enzymes are proficient catalysts: Beyond the Pauling paradigm. *Acc. Chem. Res.* **38**, 379–385 (2005).
8. D. L. Purich, *Enzyme Kinetics: Catalysis and Control: A Reference of Theory and Best-Practice Methods* (Elsevier Science, 2010).
9. J. R. Knowles, Enzyme catalysis: Not different, just better. *Nature* **350**, 121–124 (1991).
10. R. Breslow, Biomimetic chemistry and artificial enzymes: Catalysis by design. *Acc. Chem. Res.* **28**, 146–153 (1995).
11. D. J. Cram, J. M. Cram, *Container Molecules and Their Guests* (Royal Society of Chemistry, 1994).
12. D. J. Cram, H. E. Katz, I. B. Dicker, Host-guest complexation. 31. A transacylase partial mimic. *J. Am. Chem. Soc.* **106**, 4987–5000 (1984).
13. D. M. Rudkevich, G. Hilmersson, J. Rebek, Self-folding cavitands. *J. Am. Chem. Soc.* **120**, 12216–12225 (1998).

14. M. D. Nothling, Z. Xiao, A. Bhaskaran, M. T. Blyth, C. Bennett, M. L. Coote, L. A. Connal, Synthetic catalysts inspired by hydrolytic enzymes. *ACS Catalysis* **9**, 168–187 (2019).
15. H. Neurath, Proteolytic enzymes, past and future. *Proc. Natl. Acad. Sci. U.S.A.* **96**, 10962–10963 (1999).
16. O. Kirk, T. V. Borchert, C. C. Fuglsang, Industrial enzyme applications. *Curr. Opin. Biotechnol.* **13**, 345–351 (2002).
17. M. L. Bender, F. J. Kezdy, Mechanism of action of proteolytic enzymes. *Annu. Rev. Biochem.* **34**, 49–76 (1965).
18. L. Polgár, The catalytic triad of serine peptidases. *Cell. Mol. Life Sci.* **62**, 2161–2172 (2005).
19. A. R. Buller, C. A. Townsend, Intrinsic evolutionary constraints on protease structure, enzyme acylation, and the identity of the catalytic triad. *Proc. Natl. Acad. Sci. U.S.A.* **110**, E653–E661 (2013).
20. L. Polgár, Structure and function of serine proteases, in *New Comprehensive Biochemistry*, A. Neuberger, K. Brocklehurst, Eds. (Elsevier, Amsterdam, The Netherlands, 1987), chap. 3, vol. 16, pp. 159–200.
21. R. Wieczorek, K. Adamala, T. Gasperi, F. Polticelli, P. Stano, Small and random peptides: An unexplored reservoir of potentially functional primitive organocatalysts. The case of seryl-histidine. *Life* **7**, 19 (2017).
22. R. Ménard, A. C. Storer, Oxyanion hole interactions in serine and cysteine proteases. *Biol. Chem. Hoppe Seyler* **373**, 393–400 (1992).
23. A. J. Barrett, J. F. Woessner, N. D. Rawlings, *Handbook of Proteolytic Enzymes* (Elsevier Science, London, United Kingdom, 2012).
24. C. J. Hawker, K. L. Wooley, The convergence of synthetic organic and polymer chemistries. *Science* **309**, 1200–1205 (2005).
25. Y. Chi, S. T. Scroggins, J. M. J. Fréchet, One-pot multi-component asymmetric cascade reactions catalyzed by soluble star polymers with highly branched non-interpenetrating catalytic cores. *J. Am. Chem. Soc.* **130**, 6322–6323 (2008).
26. M. D. Nothling, A. Ganesan, K. Condic-Jurkic, E. Pressly, A. Davalos, M. R. Gotrik, Z. Xiao, E. Khoshdel, C. J. Hawker, M. L. O'Mara, M. L. Coote, L. A. Connal, Simple design of an enzyme-inspired supported catalyst based onacatalytic triad. *Chem* **2**, 732–745 (2017).
27. Y. Liu, S. Pujals, P. J. M. Stals, T. Paulöhrl, S. I. Presolski, E. W. Meijer, L. Albertazzi, A. R. A. Palmans, Catalytically active single-chain polymeric nanoparticles: Exploring their functions in complex biological media. *J. Am. Chem. Soc.* **140**, 3423–3433 (2018).
28. H. Rothfuss, N. D. Knöfel, P. W. Roesky, C. Barner-Kowollik, Single-chain nanoparticles as catalytic nanoreactors. *J. Am. Chem. Soc.* **140**, 5875–5881 (2018).
29. J. H. Fendler, E. J. Fendler, *Catalysis in Micellar and Macromolecular Systems* (Academic Press, NewYork, 1975).
30. C. A. Bunton, F. Nome, F. H. Quina, L. S. Romsted, Ion binding and reactivity at charged aqueous interfaces. *Acc. Chem. Res.* **24**, 357–364 (1991).
31. C. J. O'Connor, R. E. Ramage, A. J. Porter, Surfactant systems asenzyme models. *Adv. Colloid Interface Sci.* **15**, 25–70 (1981).
32. S. Ta§cioğlu, Micellar solutions as reaction media. *Tetrahedron* **52**, 11113–11152 (1996).
33. T. Kunitake, Y. Okahata, T. Sakamoto, Multifunctional hydrolytic catalyses. 8. Remarkable acceleration of the hydrolysis of p-nitrophenyl acetate by micellar bifunctional catalysts. *J. Am. Chem. Soc.* **98**, 7799–7806 (1976).
34. T. Kunitake, S. Shinkai, Catalysis by micelles, membranes and other aqueous aggregates as models of enzyme action. *Adv. Phys. Org. Chem.* **17**, 435–487 (1980).
35. Y. Ihara, M. Nango, Y. Kimura, N. Kuroki, Multifunctional micellar catalysis as a model of enzyme action. *J. Am. Chem. Soc.* **105**, 1252–1255 (1983).
36. U. Tonellato, Catalysis of ester hydrolysis by cationic micelles of surfactants containing the imidazole ring. *J. Chem. Soc. Perkin Trans. 2* **1976**, 771–776 (1976).
37. U. Tonellato, Functional micellar catalysis. Part 2. Ester hydrolysis promoted by micelles containing the imidazole ring and the hydroxy-group. *J. Chem. Soc. Perkin Trans. 2* **1977**, 821–827 (1977).
38. A. F. Abdel-Magid, K. G. Carson, B. D. Harris, C. A. Maryanoff, R. D. Shah, Reductive amination of aldehydes and ketones with sodium triacetoxyborohydride. Studies on direct and indirect reductive amination procedures[1]. *J. Org. Chem.* **61**, 3849–3862 (1996).
39. E. J. Corey, M. J. Grogan, Enantioselective synthesis of α-amino nitriles from N-benzhydryl imines and HCN with a chiral bicyclic guanidine as catalyst. *Org. Lett.* **1**, 157–160 (1999).
40. R. C. Pratt, B. G. G. Lohmeijer, D. A. Long, R. M. Waymouth, J. L. Hedrick, Triazabicyclodecene: Asimple bifunctional organocatalyst for acyl transfer and ring-opening polymerization ofcyclic esters. *J. Am. Chem. Soc.* **128**, 4556–4557 (2006).
41. N. J. V. Lindgren, L. Geiger, J. Razkin, C. Schmuck, L. Baltzer, Downsizing of enzymes by chemical methods: Arginine mimics with low pKa values increase the rates of hydrolysis of RNA model compounds. *Angew. Chem. Int. Ed.* **48**, 6722–6725 (2009).
42. M. Miyake, K. Yamada, N. Oyama, Self-assembling of guanidine-type surfactant. *Langmuir* **24**, 8527–8532 (2008).
43. S. El Hankari, P. Hesemann, Guanidinium vs ammonium surfactants in soft-templating approaches: Nanostructured silica and zwitterionic i-silica from complementary precursor–surfactant ion pairs. *Eur. J. Inorg. Chem.* **2012**, 5288–5298 (2012).
44. F. M. Menger, M. Ladika, Origin of rate accelerations in an enzyme model: The p-nitrophenyl ester syndrome. *J. Am. Chem. Soc.* **109**, 3145–3146 (1987).
45. M. L. Bender, M. J. Gibian, D. J. Whelan, The alkaline pH dependence of chymotrypsin reactions: Postulation of a pH-dependent intramolecular competitive inhibition. *Proc. Natl. Acad. Sci. U.S.A.* **56**, 833–839 (1966).
46. F. Richter, R. Blomberg, S. D. Khare, G. Kiss, A. P. Kuzin, A. J. T. Smith, J. Gallaher, Z. Pianowski, R. C. Helgeson, A. Grjasnow, R. Xiao, J. Seetharaman, M. Su, S. Vorobiev, S. Lew, F. Forouhar, G. J. Kornhaber, J. F. Hunt, G. T. Montelione, L. Tong, K. N. Houk, D. Hilvert, D. Baker, Computational design of catalytic dyads andoxyanion holes forester hydrolysis. *J. Am. Chem. Soc.* **134**, 16197–16206 (2012).
47. P. Nieri, S. Carpi, S. Fogli, B. Polini, M. C. Breschi, A. Podestà, Cholinesterase-like organocatalysis by imidazole and imidazole-bearing molecules. *Sci. Rep.* **7**, 45760 (2017).
48. A. J. Kirby, R. E. Marriott, Mechanism of RNA cleavage by imidazole. Catalysis vs medium effects. *J. Am. Chem. Soc.* **117**, 833–834 (1995).
49. R. Breslow, How do imidazole groups catalyze the cleavage of RNA in enzyme models and in enzymes? Evidence from "negative catalysis". *Acc. Chem. Res.* **24**, 317–324 (1991).
50. H. Tsukada, D. M. Blow, Structure of α-chymotrypsin refined at 1.68 Å resolution. *J. Mol. Biol.* **184**, 703–711 (1985).
51. S. C. Zimmerman, J. S. Korthals, K. D. Gramer, Syn and anti-oriented imidazole carboxylates as models for the histidine-aspartate couple in serine proteases and other enzymes. *Tetrahedron* **47**, 2649–2660 (1991).
52. T. C. Bruice, R. Lapinski, Imidazole catalysis. IV.[1] The reaction of general bases with p-nitrophenyl acetate in aqueous solution. *J. Am. Chem. Soc.* **80**, 2265–2267 (1958).
53. S. L. Johnson, General base and nucleophilic catalysis of ester hydrolysis and related reactions. *Adv. Phys. Org. Chem.* **5**, 237–330 (1967).
54. W. P. Jencks, *Catalysis in Chemistry and Enzymology* (Dover, 1987).
55. D. M. Blow, Structure and mechanism of chymotrypsin. *Acc. Chem. Res.* **9**, 145–152 (1976).
56. K. Adamala, J. W. Szostak, Competition between model protocells driven by an encapsulated catalyst. *Nat. Chem.* **5**, 495–501 (2013).
57. F. M. Menger, C. E. Portnoy, Chemistry of reactions proceeding inside molecular aggregates. *J. Am. Chem. Soc.* **89**, 4698–4703 (1967).
58. S. E. Felder, M. J. Redding, A. Noel, S. M. Grayson, K. L. Wooley, Organocatalyzed ROP of a glucopyranoside derived five-membered cyclic carbonate. *Macromolecules* **51**, 1787–1797 (2018).
59. J. Chen, J. Hao, Molecular dynamics simulation of cetyltrimethylammonium bromide and sodium octyl sulfate mixtures: Aggregate shape and local surfactant distribution. *Phys. Chem. Chem. Phys.* **15**, 5563–5571 (2013).
60. A. Dominguez, A. Fernandez, N. Gonzalez, E. Iglesias, L. Montenegro, Determination of critical micelle concentration of some surfactants by three techniques. *J. Chem. Educ.* **74**, 1227 (1997).
61. G. Dutheuil, M. P. Webster, P. A. Worthington, V. K. Aggarwal, Stereocontrolled synthesis ofcarbon chains bearing contiguous methyl groups by iterative boronic ester homologations: Application to the total synthesis of (+)-faranal. *Angew. Chem. Int. Ed. Engl.* **48**, 6317–6319 (2009).
62. M. J. Frisch, G. W. Trucks, H. B. Schlegel *et al.*, GAUSSIAN 16, Revision A.03, Gaussian, Inc., Wallingford, CT, 2009.
63. Y. Zhao, D. G. Truhlar, The M06 suite of density functionals for main group thermochemistry, thermochemical kinetics, noncovalent interactions, excited states, and transition elements: Two new functionals and systematic testing of four M06-class functionals and 12 other fun. *Theor. Chem. Acc.* **120**, 215–241 (2007).
64. A. V. Marenich, C. J. Cramer, D. G. Truhlar, Universal Solvation Model Based on Solute Electron Density and on a Continuum Model of the Solvent Defined by the Bulk Dielectric Constant and Atomic Surface Tensions. *J. Phys. Chem. B.* **113**, 6378–6396 (2009).
65. I. M. Alecu, J. Zheng, Y. Zhao, D. G. Truhlar, Computational thermochemistry: Scale factor databases and scale factors for vibrational frequencies obtained from electronic model chemistries. *J. Chem. Theory Comput.* **6**, 2872–2887 (2010).
66. N. Schmid, A. P. Eichenberger, A. Choutko, S. Riniker, M. Winger, A. E. Mark, W. F. van Gunsteren, Definition and testing of the GROMOS force-field versions 54A7 and 54B7. *Eur. Biophys. J.* **40**, 843–856 (2011).
67. M. J. Abraham, T. Murtola, R. Schulz, S. Páll, J. C. Smith, B. Hess, E. Lindahl, GROMACS: High performance molecular simulations through multi-level parallelism from laptops to supercomputers. *SoftwareX* **1–2**, 19–25 (2015).
68. K. B. Koziara, M. Stroet, A. K. Malde, A. E. Mark, Testing and validation of the automated topology builder (ATB) version 2.0: Prediction of hydration free enthalpies. *J. Comput. Aided Mol. Des.* **28**, 221–233 (2014).
69. U. Essmann, L. Perera, M. L. Berkowitz, T. Darden, H. Lee, L. G. Pedersen, A smooth particle mesh Ewald method. *J. Chem. Phys.* **103**, 8577–8593 (1995).
70. G. Bussi, D. Donadio, M. Parrinello, Canonical sampling through velocity rescaling. *J. Chem. Phys.* **126**, 014101 (2007).
71. B. Hess, P-LINCS: A Parallel Linear Constraint Solver for Molecular Simulation. *J. Chem. Theory Comput.* **4**, 116–122 (2008).

72. W. Humphrey, A. Dalke, K. Schulten, VMD: Visual molecular dynamics. *J. Mol. Graph.* **14**, 33–38 (1996).
73. R. T. McGibbon, K. A. Beauchamp, M. P. Harrigan, C. Klein, J. M. Swails, C. X. Hernández, C. R. Schwantes, L.-P. Wang, T. J. Lane, V. S. Pande, MDTraj: A modern open library for the analysis of molecular dynamics trajectories. *Biophys. J.* **109**, 1528–1532 (2015).
73. A. Prlić, A. R. Bradley, J. M. Duarte, P. W. Rose, A. S. Rose, Y. Valasatava, NGL viewer: Web-based molecular graphics for large complexes. *Bioinformatics* **34**, 3755–3758 (2018).

Acknowledgments
Funding: Funding from the U.S. Army International Technology Centre Pacific ITC-PAC FA5209-14-C-0017 and the Australian Research Council (ARC)(DP200100535) is gratefully acknowledged (to L.A.C. and M.L.O.). M.D.N. and L.A.C. acknowledge the Australia Science Endowment Fund (SIEF) for a John Stoker postgraduate Scholarship, as well as an Endeavour Research Fellowship and Australian Nanotechnology Network Overseas Travel Fellowship (to M.D.N.). M.L.C. acknowledges financial support from the ARC Centre of Excellence for Electromaterials Science (CE140100012), an ARC Laureate Fellowship (FL170100041), and supercomputing time from the National Computational Infrastructure. **Author contributions:** M.D.N., Z.X., A.B., A.E.-G., K.N., and T.B. conducted the synthesis and catalysis studies. M.A.-S. conducted the NMR studies. J.W. conducted the XRD studies. N.S.H. and M.T.B. conducted the computational studies. M.D.N., F.S., M.L.O., M.L.C., and L.A.C. conceived the concepts and designed the experiments. All authors contributed to the manuscript preparation and editing. **Competing interests:** The authors declare that they have no competing interests. **Data and materials availability:** All data needed to evaluate the conclusions in the paper are present in the paper and/or the Supplementary Materials. Additional data related to this paper may be requested from the authors.

Submitted 7 August 2019
Accepted 8 January 2020
Published 1 April 2020
10.1126/sciadv.aaz0404

Citation: M. D. Nothling, Z. Xiao, N. S. Hill, M. T. Blyth, A. Bhaskaran, M.-A. Sani, A. Espinosa-Gomez, K. Ngov, J. White, T. Buscher, F. Separovic, M. L. O'Mara, M. L. Coote, L. A. Connal, A multifunctional surfactant catalyst inspired by hydrolases. *Sci. Adv.* **6**, eaaz0404 (2020).

Science Advances

A multifunctional surfactant catalyst inspired by hydrolases

Mitchell D. Nothling, Zeyun Xiao, Nicholas S. Hill, Mitchell T. Blyth, Ayana Bhaskaran, Marc-Antoine Sani, Andrea Espinosa-Gomez, Kevin Ngov, Jonathan White, Tim Buscher, Frances Separovic, Megan L. O'Mara, Michelle L. Coote and Luke A. Connal

Sci Adv **6** (14), eaaz0404.
DOI: 10.1126/sciadv.aaz0404

Science Advances (ISSN 2375-2548) is published by the American Association for the Advancement of Science, 1200 New York Avenue NW, Washington, DC 20005. The title *Science Advances* is a registered trademark of AAAS.